Gunjan Sharma[1], *Madhu Gupta*[1*], *Ajay Sharma*[1], *Diksha Gupta*[2]

ENHANCING EFFECTIVE THERMAL CHARACTERISTICS OF NANOFLUID FLOW: INVESTIGATING THE IMPACT OVER A SHRINKING SHEET BY RESPONSE SURFACE METHODOLOGY

POBOLJŠANJE KARAKTERISTIKA TOPLOTNE EFIKASNOSTI PROTOKA NANOFLUIDA: ISTRAŽIVANJE UTICAJA PREKO SKUPLJAJUĆE FOLIJE METODOLOGIJOM ODZIVNIH POVRŠINA

Originalni naučni rad / Original scientific paper
Rad primljen / Paper received: 15.04.2026
https://doi.org/10.69644/ivk-2026-siB-0033

Adresa autora / Author's address:
[1] Chitkara University School of Engineering and Technology, Chitkara University, Himachal Pradesh, 174103, India
G. Sharma https://orcid.org/0009-0000-7785-2250 ;
M. Gupta https://orcid.org/0000-0001-5062-2199 ;
A. Sharma https://orcid.org/0000-0002-6816-7240
[2] Math and Science Department, University of Technology Bahrain, Salmabad, 18041, Kingdom of Bahrain
D. Gupta https://orcid.org/0009-0005-1104-5014
*email: madhu.gupta@chitkarauniversity.edu.in

Keywords
- nanofluid
- thermal radiation
- finite element method
- response surface methodology

Abstract

The objective of this study to propose a methodology to examine nanofluids flow enhanced thermal conductivity and heat transfer behaviour. The study aims to depict the optimised parameter values at which enhanced thermal conductivity of nanofluids results in more efficient cooling. To achieve this, mixed convection nanofluid (Cu-water) flow over a shrinking sheet under radiative effects is investigated numerically using finite element method (FEM). The analysis incorporates key parameters such as the suction, thermal conductivity, radiation and mixed convection which govern the flow and heat transfer characteristics. The numerical investigation depicts that suction is the most dominant factor which helps to reduce the boundary layer thickness and enhance heat transfer. Radiative effects lead to a thicker thermal boundary layer that consequently reduces the heat transfer rate. The mixed convection parameter also contributes to higher heat transfer rate, simultaneously increasing the skin friction. Corresponding diagrams are plotted to illustrate the outcomes. Results show that the nanofluid model developed in this work exhibits higher Nusselt number as compared to the base microfluid model, confirming improved heat transfer. Also, results obtained statistically by Response Surface Methodology (RSM) using MATLAB® are investigated for optimised value of parameters. The results from the RSM model show a strong positive correlation with our numerical FEM results. The RSM-ANOVA optimisation reveals a strong correlation, giving accuracy of 0.975, highlighting the roles of suction and radiative heat transfer in determining thermal behaviour. This study provides insights for effective thermal management in thin-film manufacturing processes.

Ključne reči
- nanofluid
- toplotno zračenje
- metoda konačnih elemenata
- metodologija odzivnih površina

Izvod

Cilj ovog rada je u predstavljanju metodologije za proučavanje protoka nanofluida povećane toplotne provodljivosti i ponašanja prenosa toplote. Otkrivaju se vrednosti optimizovanih parametara sa kojima poboljšana toplotna provodljivost nanofluida dovodi do efikasnijeg hlađenja. Da bi ovo postigli, proučavamo numerički (metodom konačnih elemenata - MKE) protok mešavine nanofluida (Cu-voda) preko folije koja se skuplja, u uslovima zračenja. Analizom su obuhvaćeni ključni parametri, kao što su usisavanje, toplotna provodljivost, zračenje i konvekcija mešavine, kojima se definišu karakteristike protoka i prenosa toplote. Numeričkim istraživanjem se pokazuje da je usisavanje najdominantniji faktor kojima se postiže smanjenje debljina graničnog sloja i poboljšava prenos toplote. Uticaji zračenja dovode do debljeg toplotnog graničnog sloja, kojim se smanjuje brzina prenosa toplote. Parametar konvekcije mešavine takođe doprinosi povećanju brzine prenosa toplote, sa istovremenim povećanjem trenja graničnog sloja. Dati su odgovarajući dijagrami koji ilustruju rezultate. Rezultati pokazuju da model nanofluida razvijen u radu ima povećan Nuseltov broj u poređenju sa osnovnim modelom mikrofluida, čime se potvrđuje poboljšanje prenosa toplote. Takođe, statistički rezultati dobijeni metodologijom odzivnih površina (RSM) korišćenjem MATLAB® su obrađeni radi optimizacije parametara. Rezultati RSM modela pokazuju jače pozitivno poklapanje sa numeričkim rezultatima MKE. RSM-ANOVA optimizacija daje bolje poklapanje, sa tačnošću 0.975, čime se ističu uloge usisavanja i prenosa toplote zračenjem, u oceni ponašanja prenosa toplote. Rad daje uvid u efikasno upravljanje prenosom toplote kod proizvodnih procesa taloženja sa tankim filmom.

INTRODUCTION

Thin-film coating processes as metal deposition, thin film manufacturing, metal and polymer coating requires effective thermal control to ensure uniform coating and stable film structure. The heat removal process during film formation or cooling can be enhanced by studying the effects of parameters mixed convection, suction and radiation for effective thermal management. By optimising these parameters, the overall cooling performance of the thin-film layer can be significantly enhanced. Abbas et al. /1/ analysed thermal radiation parameter with a positive effect on temperature distribution over stretching/shrinking sheets. Thermal radiation effects over shrinking/stretching sheets have also been studied by Abdel et al. /2/. Temperature and velocity profiles analysis over the boundary layers has been examined in /3/. Thermal enhancement in hybrid nanofluid flow over inclined thin surface is analysed by Alharbi et al. /4/. Nanofluid flow and heat transfer in thin films over stretching surfaces under the influence of suction and radiation is done by Alrehili et al. /5/, along with other authors /6-7/ that have also studied effects of thermal radiation over different geometries. The authors have examined the effects of heat transfer in the presence of radiation combining various parameters such as magnetic effects, permeability, heat transfer to obtain significantly higher thermal conductivity in various industrial systems /8/. Analysis of Newtonian fluids under slip conditions has been studied by Evans et al. /9/. Gonsalves et al. /10/ analysed heat transfer in nanofluids considering convective boundary conditions using the finite element method. Mixed convection flow under the effects of radiation is studied by Gupta et al. /11/. Hady et al. /12/ studied radiation parameter in a nanofluid over a nonlinearly stretching sheet and observed that radiation parameter increases the thermal boundary layer thickness and reduces Nusselt number. Heat transfer is investigated by Hafeez et al. /13/ in a radiative hybrid fluid flowing over a wedge surface. Also, the study has been extended to unsteady nanofluid flows by Hayat and Shahzad /14/ over radially stretching sheets. Ishaq et al. /15/ studied two-dimensional nanofluid flow considering heat and mass transfer in the existence of uniform magnetic field and radiation over an unsteady porous stretching sheet. Hussain et al. /16/ examined micropolar fluid for boundary layer flow over stretching/shrinking sheet. Kamis et al. /17/ investigated the thin film convective boundary layer in the presence of suction and injection. Comprehensive review of nanofluids is studied by Nabwey et al. /18/. Naseem and Shahzad /19/ analysed heat transfer and nanofluid flow in thin films over an unsteady stretching sheet under the effects of entropy generation. These studies motivate the study and application of numerical methods in nanofluid flows over shrinking sheet. Variable properties of micropolar fluid are investigated by Saraswathy et al. /20/. Thermal radiation and magnetic field over effects over nonlinear shrinking porous sheets is examined in /21/. Galerkin finite element method is employed to compare the performance of nanofluids by Sohail et al. /22/. Ullah et al. /23/ investigate thin film flow of nanofluids considering the effects of thermophoresis and Brownian motion under uniform magnetic field. Venkata Ramana Reddy et al. /24/ consider the thermal radiation and convective boundary conditions. Vrionis et al. /25/ develop a thin film flow approximation solver under the effect of environmental heterogeneities. In addition, the micropolar flow is investigated over a shrinking sheet in study done by Yacob and Ishak /26/. Zainal et al. /27/ examined velocity slip condition at the boundary resulting in reduced skin friction coefficient. The present work considers a steady two-dimensional nanofluid flow over a permeable shrinking sheet with thermal radiation and mixed convection effects. Initially, FEM is employed to solve the governing equations of the physical model, after which RSM is utilised to develop a predictive model and perform a multi-objective optimisation of the system's performance. Thus, the present study highlights that the cooling performance of shrinking sheets is influenced by combined effects of radiation and the thermophysical properties of the nanofluid.

MATHEMATICAL MODEL

Consider a two-dimensional steady flow of a nanofluid over a permeable shrinking sheet, representing thermal cooling operations in thin-film manufacturing. The *x*-axis is assumed to be along the sheet and the *y*-axis normal to it; the velocity components of the nanofluid are $u = -U(x)$ and $v = V_w$ (wall velocity). The sheet temperature is T_w and the temperature far away from the sheet is T_∞ (Fig. 1). Suction at the sheet is employed to stabilise the boundary layer, while the shrinking sheet simulates the dynamic motion of thin films during cooling. The nanofluid is assumed to be incompressible and viscous, neglecting pressure gradients and nanoparticle interactions with the surroundings. Primary parameters of the study are Nusselt number and the skin-friction coefficient, which govern surface shear and heat flux to achieve uniform cooling and prevent thermal distortion in sheet-based manufacturing processes.

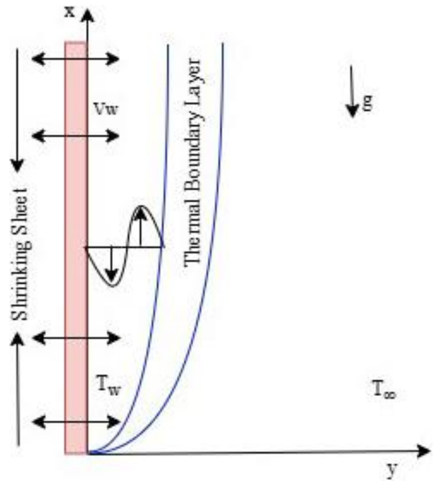

Figure 1. Physical model and coordinate system.

To model the steady boundary layer flow of nanofluid, the continuity, momentum and energy, the equation can be formulated under assumptions of Boussinesq and boundary layer approximations governed by continuity, linear momentum and energy equations, respectively, as follows:

$$\frac{\partial u}{\partial x}+\frac{\partial v}{\partial y}=0\,, \tag{1}$$

$$u\frac{\partial u}{\partial x}+v\frac{\partial v}{\partial y}=\frac{\mu_{nf}}{\rho_{nf}}\frac{\partial^2 u}{\partial y^2}+\frac{(\rho\beta)_{nf}}{\rho_{nf}}(T-T_\infty)g\,, \tag{2}$$

$$u\frac{\partial T}{\partial x}+v\frac{\partial T}{\partial y}=\alpha_{nf}\frac{\partial^2 T}{\partial y^2}-\frac{1}{(\rho C_p)_{nf}}\frac{\partial q_r}{\partial y}\,, \tag{3}$$

where: g is acceleration due to gravity; q_r is radiative heat flux; *nf* denotes nanofluid, and parameters of nanofluids are: μ_{nf} dynamic viscosity; ρ_{nf} density; $(\rho\beta)_{nf}$ thermal expansion coefficient; $(\rho C_p)_{nf}$ heat capacitance; α_{nf} thermal diffusivity; q_r radiative heat flux; and ν_{nf} kinematic viscosity.

The relevant velocity and temperature boundary conditions over a shrinking sheet are:

at $y = 0$: $u = -U(x)$, $v = V_w$, $T = T_w$ and
as $y \to \infty$: $u \to 0$, $T \to T_\infty$. (4)

Nanofluid properties appearing in governing equations are expressed using the following relations /10/:

$$\rho_{nf} = (1-\phi)\rho_f + \phi\rho_{s*},$$
$$(\rho C_p)_{nf} = (1-\phi)(\rho C_p)_f + \phi(\rho C_p)_{s*},$$
$$(\rho\beta)_{nf} = (1-\phi)(\rho\beta)_f + \phi(\rho\beta)_{s*},$$
$$\frac{k_{nf}}{k_f} = \frac{k_{s*} + 2k_f - 2\phi(k_f - k_{s*})}{k_{s*} + 2k_f + \phi(k_f - k_{s*})},$$
$$\mu_{nf} = \frac{\mu_f}{(1-\phi)^{2.5}}. \tag{5}$$

Here, k_{nf} is the thermal conductivity of the nanofluid. Subscripts f denote the base fluid, and s^* denotes solid nanoparticles, so ρ_{s*} is the density of nanoparticles; ρ_f is density of the base fluid; ϕ is the volume fraction of nanoparticles; μ_f is dynamic viscosity of the base fluid.

Under the effects of radiation, the Rosseland's approximation for the radiative heat flux vector q_r is given by /11/:

$$q_r = \frac{-4\sigma x}{3k^*}\frac{\partial T^4}{\partial y}. \tag{6}$$

Here, k^* is Rosseland mean spectral absorption coefficient, and σ^* represents the Stefan-Boltzmann constant. The variation in temperature within the flow is assumed to be adequately small such that T^4 can be represented as a linear function of temperature. This is achieved by expanding T^4 in a Taylor series about T_∞ and omitting higher-order terms:

$$T^4 \approx 4T_\infty^3 T - 3T_\infty^4. \tag{7}$$

On substituting Eqs.(5), (6) and (7) into the energy Eq.(3), we get the following:

$$u\frac{\partial T}{\partial x} + v\frac{\partial T}{\partial y} = \left(\alpha_{nf} + \frac{16\sigma^* T_\infty^3}{3k^*(\rho C_p)_{nf}}\right)\frac{\partial^2 T}{\partial y^2}. \tag{8}$$

Velocity components can be expressed in terms of the stream function ψ as:

$$u = \frac{\partial\psi}{\partial y} \quad \text{and} \quad v = -\frac{\partial\psi}{\partial x}. \tag{9}$$

Introducing non-dimensional similarity variables to transform the governing partial differential equations:

$$\eta = y\sqrt{a/v_f}, \ \psi(x,y) = \sqrt{av_f}\, xf(\eta), \ \theta(\eta) = \frac{T - T_\infty}{T_w - T_\infty}. \tag{10}$$

The nonlinear partial momentum differential Eq.(2) and energy Eq.(3) get reduced to a set of nonlinear ordinary differential equations as below:

$$Kf''' + K_1(ff'' - (f'^2)) + K_2\theta = 0, \tag{11}$$
$$K_3\theta'' + K_4 f\theta' = 0, \tag{12}$$

where values of K, K_1, K_2, K_3 and K_4 are obtained as

$$K = \frac{1}{(1-\phi)^{2.5}}, \quad K_1 = 1 - \phi + \frac{\phi\rho_s}{\rho_f},$$
$$K_2 = 1 - \phi + \phi\left(\frac{\rho\beta_s}{\rho\beta_f}\right), \quad K_3 = \frac{K_{nf}}{K_f} + \frac{4N_r}{3},$$
$$K_4 = \Pr\left((1-\phi) + \frac{\phi(\rho C_p)_s}{(\rho C_p)_f}\right). \tag{13}$$

Also, similarity transformations reduce boundary conditions Eq.(4) to:

$$f(0) = s, \ f'(0) = -1, \ \theta(0) = 1,$$
$$f'(\eta) \to 0, \ \theta(\eta) \to 0, \ \text{as} \ \eta \to \infty. \tag{14}$$

The dimensionless parameters are Prandtl number Pr, radiation parameter N_r, Grashof number Gr, Reynolds number Re. The mixed convection parameter λ is defined as the ratio of the Grashof and Reynolds numbers:

$$\lambda = \frac{\mathrm{Gr}}{\mathrm{Re}^2} = \frac{g\beta_f(T_w - T_\infty)}{a^2 x}. \tag{15}$$

The skin friction coefficient C_f and Nusselt number Nu are significant physical quantities in our study:

$$C_f = \frac{\tau_w}{\rho_f U^2}, \quad \mathrm{Nu} = \frac{xq}{k_f(T_w - T_\infty)}. \tag{16}$$

The shear stress at the wall τ_w and the constant surface heat flux q are given by:

$$\tau_w = \mu_{nf}\left(\frac{\partial u}{\partial y}\right)_{y=0}, \ q = -k_{nf}\left(\frac{\partial T}{\partial y}\right)_{y=0} - \left(\frac{4\sigma^*}{3k^*}\frac{\partial T^4}{\partial y}\right)_{y=0}. \tag{17}$$

Using similarity transformations in Eq.(10) and values of parameters from Eqs.(15) and (16), follows as:

$$\mathrm{Re}^{1/2} C_f = \frac{1}{(1-\phi)^{2.5}} f''(0),$$
$$\mathrm{Re}^{-1/2}\,\mathrm{Nu} = -\left(\frac{k_{nf}}{k_f} + \frac{4}{3}N_r\right)\theta'(0). \tag{18}$$

FINITE ELEMENT FORMULATION

To solve nonlinear equations, we reduce the third-order Eqs.(11) and (12) by considering $h = f'$. Now, the system of reduced equations is given by:

$$f' - h = 0,$$
$$Kh'' + K_1(fh' - h^2) + K_2\theta = 0,$$
$$K_3\theta'' + K_4 f\theta' = 0, \tag{19}$$

and transformed boundary conditions as

$$f(0) = s, \ h(0) = -1, \ \theta(0) = 1,$$
$$h(\eta) \to 0, \ \theta(\eta) \to 0 \ \text{as} \ \eta \to \infty. \tag{20}$$

The variational form of Eq.(19) over element (η_e, η_{e+1}) is given by:

$$\int_{\eta_e}^{\eta_{e+1}} w_1(f' - h)\,d\eta = 0,$$
$$\int_{\eta_e}^{\eta_{e+1}} w_2(Kh'' + K_1(fh' - h^2) + K_2\theta)\,d\eta = 0,$$
$$\int_{\eta_e}^{\eta_{e+1}} w_3(K_3\theta'' + K_4 f\theta')\,d\eta = 0. \tag{21}$$

Here, wi_1, w_2 and w_3 are linearly independent weight functions corresponding to variation in functions f, h and θ, respectively. Dividing the domain into n linear elements and assuming linear shape functions ψ_l, the finite element model is obtained from Eq.(21) by using linear approximation functions, where approximations for f, h, θ and the weight w_i over a single element are defined as:

$$f = \sum_{j=1}^{2} f_j\psi_j, \ h = \sum_{j=1}^{2} h_j\psi_j,$$
$$\theta = \sum_{j=1}^{2}\theta_j\psi_j, \ w_i = \psi_i \ \text{for} \ i = 1,2. \tag{22}$$

Introducing Lagrange's interpolation functions for a linear element on (η_e, η_{e+1}):

$$\psi_1(\eta) = \frac{\eta_{e+1} - \eta}{\eta_{e+1} - \eta_e} \quad \text{and} \quad \psi_2(\eta) = \frac{\eta - \eta_e}{\eta_{e+1} - \eta_e}. \tag{23}$$

Using these approximations, we convert Eq.(21) to form the element stiffness matrix, where the global matrix is represented in the form:

$$\begin{bmatrix} [K^{11}] & [K^{12}] & [K^{13}] \\ [K^{21}] & [K^{22}] & [K^{23}] \\ [K^{31}] & [K^{32}] & [K^{33}] \end{bmatrix} \begin{pmatrix} \{f\} \\ \{h\} \\ (\theta) \end{pmatrix} = \begin{pmatrix} \{b^1\} \\ \{b^2\} \\ \{b^3\} \end{pmatrix}. \quad (24)$$

Here, $[K^{mn}]$ are 2×2 and $\{f^m\}$, $\{b^m\}$ are 2×1 order matrices, where (m, n = 1, 2, 3). The specific element components are given by:

$$K_{ij}^{11} = \int_{\eta_e}^{\eta_{e+1}} \psi_i \frac{d\psi_j}{d\eta} d\eta,\ K_{ij}^{12} = -\int_{\eta_e}^{\eta_{e+1}} \psi_i \psi_j d\eta,\ K_{ij}^{13} = 0,\ K_{ij}^{21} = 0,$$

$$K_{ij}^{22} = -K \int_{\eta_e}^{\eta_{e+1}} \frac{d\psi_i}{d\eta} \frac{d\psi_j}{d\eta} d\eta + K_1 \int_{\eta_e}^{\eta_{e+1}} \psi_i \frac{d\psi_j}{d\eta} \bar{f} d\eta - K_1 \int_{\eta_e}^{\eta_{e+1}} \psi_i \psi_j \bar{h} d\eta,$$

$$K_{ij}^{23} = -K_2 \int_{\eta_e}^{\eta_{e+1}} \psi_i \psi_j d\eta,\ K_{ij}^{31} = 0,\ K_{ij}^{32} = 0, \quad (25)$$

$$\text{and}\ \{b_i^1\} = 0,\ \{b_i^2\} = \frac{1}{(1-\phi)^{2.5}} \psi_i \left[\frac{dh}{d\eta}\right]_{\eta_e}^{\eta_{e+1}},$$

$$\{b_i^3\} = \left(\frac{k_{nf}}{k_f} + \frac{4N_r}{3}\right) \psi_i \left[\frac{d\theta}{d\eta}\right]_{\eta_e}^{\eta_{e+1}}. \quad (26)$$

On assembling the element equations, we obtain a system of nonlinear equations which are solved iteratively. The system is linearised by assuming that the functions $\bar{f}$ and $\bar{h}$ are known at a lower iteration level. Computations for the functions f, h, and θ are then carried out for higher level. The process is repeated until the required accuracy of 0.0005 is obtained. The results of the convergence study for a different parameter set are presented in Table 1.

Table 1. Convergence study results for different values of n (Pr = 1, s = 3, N_r = 1).

n	h(1.2)	θ(1.2)
40	0.16811	0.37195
80	0.15858	0.37808
120	0.15686	0.37922
160	0.15625	0.37961
200	0.15598	0.37980
240	0.15583	0.37990
280	0.15574	0.37996
320	0.15568	0.38000
360	0.15564	0.38003
400	0.15561	0.38005
440	0.15559	0.38006
480	0.15557	0.38007
520	0.15556	0.38008
560	0.15555	0.38009
600	0.15554	0.38009
640	0.15553	0.38010
680	0.15553	0.38010

In Table 1, the convergence behaviour is observed for values of h(1.2) and θ(1.2) as the number of elements is increased from 40 to 680. The convergence in values beyond n = 600 shows that the FEM solution has reached independence validating that the mesh resolution is sufficient, and no change is observed on further refinement. This proves accuracy of numerical solutions and the independence of mesh for $n \geq 600$.

Table 2. Comparison of analytical and FEM results for $f'(\eta)$ at different η values.

η	$f'(\eta)$ analytical	FEM
0	-1.00000	-1.00000
1	-0.07295	-0.07223
2	-0.00532	-0.00522
3	-0.00039	-0.00038
4	-0.00003	-0.00003
5, 6, 7, 8	0.00000	0.00000

For the case of a viscous fluid, the exact analytical solution for the velocity gradient $f'(\eta)$ subject to the boundary conditions is given by Yacob and Ishaq /26/ as:

$$f'(\eta) = -\exp(-C\eta) \quad \text{where,}\ C = \frac{s + \sqrt{s^2 - 4}}{2}, \quad (27)$$

and s is suction parameter. The flow velocity $f'(\eta)$ values obtained by FEM and the analytical results are presented in Table 2. It is evident from the table that the numerical results obtained using the present FEM formulation are in close agreement with the analytical solution. This confirms the accuracy and validity of the present FEM results.

RESULTS AND DISCUSSION

The effect of various important parameters such as suction parameter s, mixed convection parameter λ, and radiation parameter N_r on velocity and temperature profiles are studied and shown graphically by keeping the volume fraction of the nanoparticles fixed at ϕ = 0.01, and Prandtl number Pr = 6.2, while other parameters are varied to analyse their influence on the skin-friction coefficient and Nusselt number. These results are shown in Figs. 2-7.

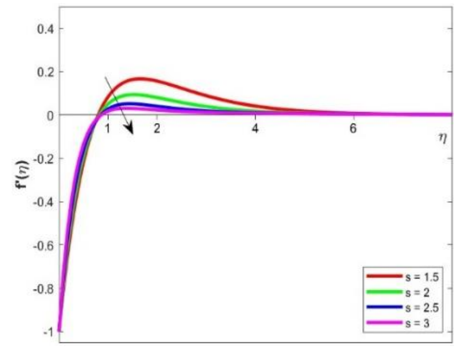

Figure 2. Velocity distribution for varying s (N_r = 0.5, λ = 1.0).

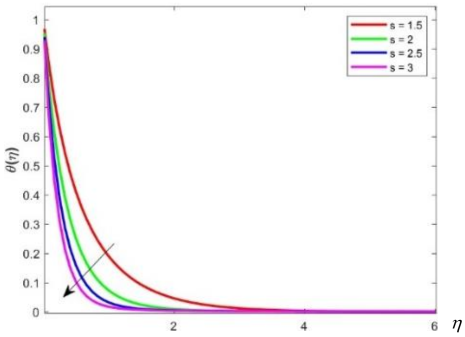

Figure 3. Temperature distribution for varying s (N_r = 0.5, λ = 0.1).

Figure 2 depicts the impact of suction parameter s on the velocity distribution as suction pulls the fluid particles closer to the surface, making the boundary layer thicker. A higher value of s reduces the velocity, keeping the flow stable on shrinking surfaces. The effect of the suction parameter s on the temperature profile $\theta(\eta)$ is depicted in Fig. 3. As suction increases, the thermal boundary layer becomes significantly thinner and the temperature gradient at the wall is reduced, indicating a higher rate of heat transfer.

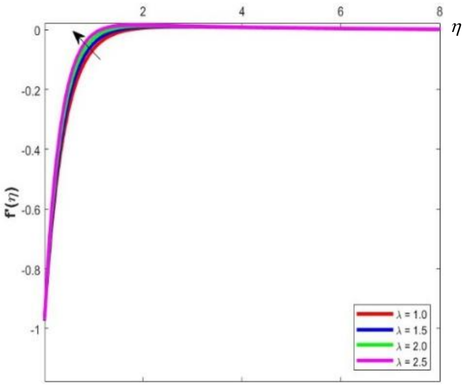

Figure 4. Velocity distribution for varying λ (s =2.5, N_r = 3.0).

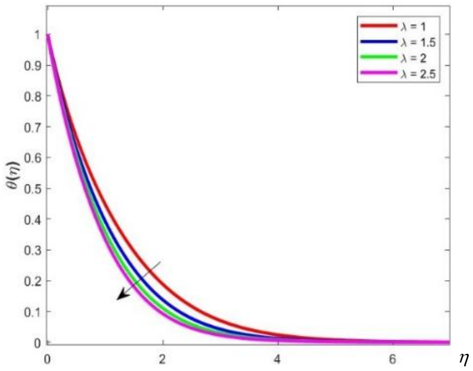

Figure 5. Temperature distribution for varying λ (N_r = 0.5, s =1.0).

The effect of mixed convection parameter λ on the velocity of a fluid is illustrated in Fig. 4. A higher value of λ causes a stronger upward push, which increases the velocity in the reverse flow region. Figure 5 depicts the effect of the mixed convection parameter λ on the temperature profile $\theta(\eta)$. A stronger buoyancy force leads to a decrease in the fluid's temperature closer to the wall, resulting in a higher rate of heat transfer.

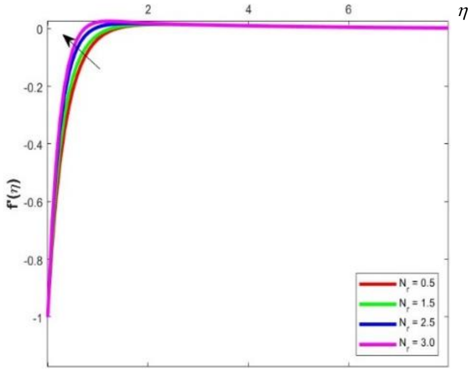

Figure 6. Velocity distribution for varying N_r (s = 3.0, λ = 5.0).

Figure 6 shows the effect of the thermal radiation parameter N_r on the velocity profile. A higher value of N_r improves fluid velocity in the boundary layer due to the influence of the mixed convection parameter. In Fig. 7, the effect of the thermal radiation parameter N_r on the temperature profile $\theta(\eta)$ is depicted. Higher thermal radiation allows heat from the hot surface to penetrate more deeply into the fluid hence, it lowers the heat transfer from the surface.

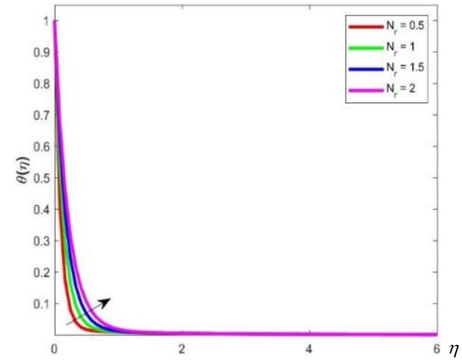

Figure 7. Temperature distribution for varying N_r (s = 3.0, λ = 5.0).

Table 3. Impact of λ, N_r and s on skin-friction coefficient $f''(0)$.

$N_r = 1, s = 5$		$\lambda = 3, s = 5$		$\lambda = 3, N_r = 1$	
λ	$f''(0)$	N_r	$f''(0)$	s	$f''(0)$
2.0	3.95139	0.5	3.96861	1.0	3.19074
2.5	4.09603	0.7	4.07698	3.0	3.81842
3.0	4.23885	1.0	4.23885	5.0	4.23885
3.5	4.37993	1.5	4.50193	7.0	4.88553
4.0	4.51934	2.0	4.75091	10.0	5.87576

The results obtained in Table 3 depict the values of the skin friction coefficient for different values of the chosen parameters. An improvement in Nusselt number is observed with increasing suction parameter, indicating enhanced surface heat transfers. This suggests that applying controlled suction through porous sheets can effectively thin the thermal boundary layer, enabling more uniform cooling. Also, higher radiation reduces the Nusselt number, highlighting the need to minimise excess thermal radiation during cooling stages.

Table 4. Impact of λ, N_r, and s on Nusselt number $\theta'(0)$.

$N_r = 1, s = 5$		$\lambda = 3, s = 5$		$\lambda = 3, N_r = 1$	
λ	$f''(0)$	N_r	$f''(0)$	s	$f''(0)$
2.0	3.95139	0.5	3.96861	1.0	3.19074
2.5	4.09603	0.7	4.07698	3.0	3.81842
3.0	4.23885	1.0	4.23885	5.0	4.23885
3.5	4.37993	1.5	4.50193	7.0	4.88553
4.0	4.51934	2.0	4.75091	10.0	5.87576

In Table 4 it is observed that as the radiation parameter N_r increases, it reduces the Nusselt number, while increase in the mixed convection parameter λ leads to increased heat transfer. The suction parameter s exhibits the most significant impact, improving heat transfer by thinning the thermal boundary layer. The numerical analysis shows that the combination of suction and convection parameters with radiation improves thermal management.

Figure 8 presents comparison of Nusselt number with the base study /10/ and shows that the introduction of nanoparticles significantly improves the thermal performance of the current model. Nusselt number shows a consistent increase with values of λ, N_r and s depicting higher values than the microfluid flow, confirming the enhanced thermal conductivity and superior heat-transfer performance of nanofluid flow.

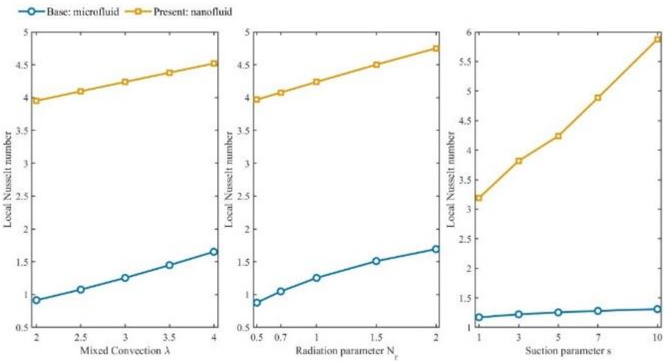

Figure 8. Comparison of Nusselt number for varying λ, N_r, and s with base study, /10/.

RESPONSE SURFACE METHODOLOGY

To study the association between various input variables and their corresponding output variables developed a hybrid method. This method uses various statistical and mathematical techniques to optimise multiple responses. RSM is used to optimise the results from the given data. In statistics, numerical and experimental designs like Box-Behnken Design and Central Composite Design (CCD) /20/ are used to calculate empirical correlations. We use CCD in this study. A second-order multivariate regression model is fitted to predict the average Nusselt number and skin friction coefficient.

Table 5. Parameter levels for CCD-RSM design.

Parameter	-1	0	1
ϕ ($0.01 \le \phi \le 0.1$)	0.01	0.05	0.10
S ($0.5 \le s \le 5.0$)	0.50	2.75	5.00
λ ($0.5 \le \lambda \le 5.0$)	0.50	2.75	5.00
N_r ($0.2 \le N_r \le 3.0$)	0.20	1.60	3.00

For this study, a total of 36 experimental runs were conducted for parameters: volume fraction ϕ, suction parameter s, mixed convection parameter λ, and radiation parameter N_r, each investigated at three levels as summarised in Table 6. The experimental design also includes responses in runs 26-36 with identical responses as obtained in run 25, hence the responses have been omitted in the table.

Experimental design is based on the factorial approach comprising 36 runs that have responses of Nusselt number and skin friction number for different governing parameters.

Table 6. Experimental design and responses.

Run	λ	N_r	s	ϕ	λ^*	N_{r*}	s^*	ϕ_*	Skin friction	Nusselt number
1	-1	-1	-1	-1	0.5	0.2	0.5	0.01	0.7558	0.1615
2	-1	-1	-1	1	0.5	0.2	0.5	0.1	0.7492	0.1118
3	-1	-1	1	-1	0.5	0.2	5	0.01	4.1378	19.547
4	-1	-1	1	1	0.5	0.2	5	0.1	4.1385	18.471
5	-1	1	-1	-1	0.5	3	0.5	0.01	0.5606	0.1135
6	-1	1	-1	1	0.5	3	0.5	0.1	0.5581	0.1135
7	-1	1	1	-1	0.5	3	5	0.01	4.1824	5.6915
8	-1	1	1	1	0.5	3	5	0.1	4.1836	5.5955
9	1	-1	-1	-1	5	0.2	0.5	0.01	1.4443	5.3705
10	1	-1	-1	1	5	0.2	0.5	0.1	1.6772	4.1413
11	1	-1	1	-1	5	0.2	5	0.01	4.1307	19.547
12	1	-1	1	1	5	0.2	5	0.1	4.1375	18.472
13	1	1	-1	-1	5	3	0.5	0.01	3.4751	0.8626
14	1	1	-1	1	5	3	0.5	0.1	3.4893	0.8536
15	1	1	1	-1	5	3	5	0.01	4.5751	5.6959
16	1	1	1	1	5	3	5	0.1	4.5872	5.6001
17	-1	0	0	0	0.5	1.6	2.75	0.055	2.279	5.6085
18	1	0	0	0	5	1.6	2.75	0.055	2.7585	5.6221
19	0	-1	0	0	2.75	0.2	2.75	0.055	2.2387	16.302
20	0	1	0	0	2.75	3	2.75	0.055	2.8574	3.3671
21	0	0	-1	0	2.75	1.6	0.5	0.055	2.2009	0.9381
22	0	0	1	0	2.75	1.6	5	0.055	4.2479	8.7153
23	0	0	0	-1	2.75	1.6	2.75	0.01	2.5131	5.7068
24	0	0	0	1	2.75	1.6	2.75	0.1	2.5288	5.5266
25	0	0	0	0	2.75	1.6	2.75	0.055	2.5209	5.6153

RSM analysis for Nusselt number (Nu): the second-order response surface model developed for the Nusselt number is given as

$$\mathrm{Nu} = \beta_0 + \beta_1\lambda + \beta_2 N_r + \beta_3 s + \beta_4\varphi + \beta_{11}\lambda^2 + \beta_{22}N_r^2 + \beta_{33}s^2 + \\ + \beta_{44}\varphi^2 + \beta_{12}\lambda N_r + \beta_{13}\lambda s + \beta_{14}\lambda\varphi + \beta_{23}sN_r + \beta_{24}N_r\varphi + \beta_{34}s\varphi \,. \quad (28)$$

Model fit statistics: number of observations 36, error degrees of freedom 21, root mean squared error 1.05, R-squared: 0.97, adjusted R-squared: 0.96, p-value ≤ 0.001.

Figures 9-11 illustrate that the Nusselt number increases moderately with increasing λ, while higher suction values s enhance heat transfer. The nanoparticle volume fraction ϕ is found to have a negligible effect on the Nusselt number. Whereas the radiation parameter N_r strongly suppresses heat transfer when combined with higher suction.

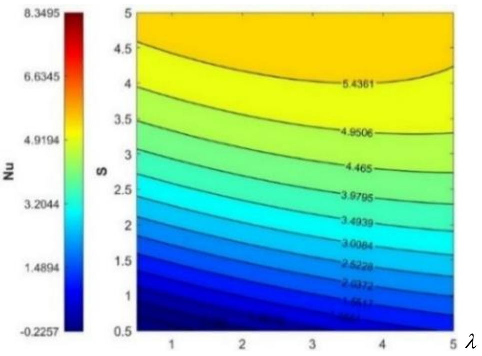

Figure 9. Contour plot for Nusselt number vs. s, λ.

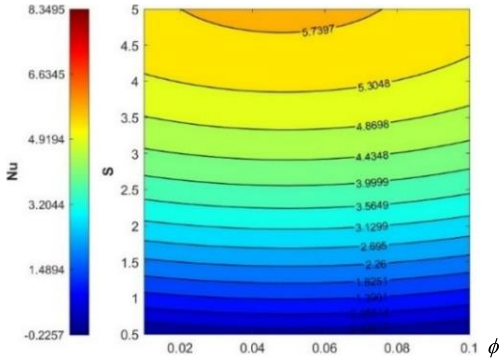

Figure 10. Contour plot for Nusselt number vs. s, ϕ.

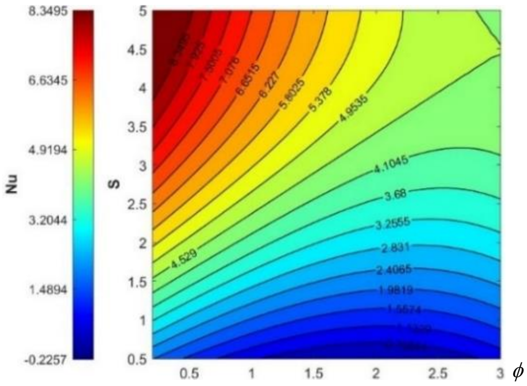

Figure 11. Contour plot for Nusselt number vs. s, ϕ.

Table 7. Coefficients estimated for Nusselt number using CCD-RSM.

Term	Estimate	SE	t-Stat	P-Value
Intercept	-0.9499	1.1801	-0.8049	0.4298
λ	1.5384	0.7536	2.0413	0.0539
N_r	-6.1628	1.1455	-5.3802	< 0.001
s	5.6649	0.7536	7.5168	< 0.001
ϕ	25.0500	37.6820	0.6647	0.5134
$\lambda : N_r$	-0.1535	0.0832	-1.8454	0.0791
$\lambda : s$	-0.1323	0.0517	-2.5550	0.0184
$\lambda : \phi$	-0.7333	2.5894	-0.2832	0.7797
$N_r : s$	-0.9050	0.0832	-10.874	< 0.001
$N_r : \phi$	3.2037	4.1615	0.7698	0.4499
$s : \phi$	-0.6515	2.5894	-0.2516	0.8037
λ^2	-0.1132	0.1282	-0.8831	0.3871
N_r^2	1.8600	0.3312	5.6148	< 0.001
s^2	-0.2690	0.1282	-2.0976	0.0482
ϕ^2	-282.480	320.6400	-0.8809	0.3883

The RSM analysis of the Nusselt number in Table 7 demonstrates that the suction parameter s has the most significant positive effect on the Nusselt number. While the radiation parameter N_r has negative effects. The mixed convection parameter λ shows a moderate positive effect, while the nanoparticle volume fraction ϕ does not significantly impact heat transfer. The linear interaction term, $N_r : s$ is highly significant, showing that radiation strongly reduces the positive effect of suction. Quadratic effects confirm a nonlinear relationship between these parameters and heat transfer.

Table 8. ANOVA results for the Nusselt number response.

Source	SumSq	DF	MeanSq	F-value	P-Value
Total	1016.80	35	29.05		
Model	993.70	14	70.97	64.53	< 0.001
Linear	811.26	4	202.81	184.41	< 0.001
Nonlinear	182.44	10	18.24	16.58	< 0.001
Residual	23.09	21	1.09		
Lack of fit	23.09	10	2.30	-	
Pure error	0	11	0		

Table 8 of ANOVA provides the significance of the response surface model for the Nusselt number. The overall model is highly significant with an F-value of 64.539 and a P-value < 0.001, indicating that the variation explained by the model is much greater than the residual error. Linear terms contribute the most to the model, dominating the response behaviour. Also, the curvature and interaction effects show the interaction of nonlinear terms. The residual error is very small, indicating that the model fits the data well and is suitable for prediction and optimisation.

RSM Analysis for skin friction ($f''(0)$): the second-order response surface model developed for skin friction is given as

$$f''(0) = \beta_0 + \beta_1\lambda + \beta_2 N_r + \beta_3 s + \beta_4\varphi + \beta_{11}\lambda^2 + \beta_{22}N_r^2 + \beta_{33}s^2 + \\ + \beta_{44}\varphi^2 + \beta_{12}\lambda N_r + \beta_{13}\lambda s + \beta_{14}\lambda\varphi + \beta_{23}sN_r + \beta_{24}N_r\varphi + \beta_{34}s\varphi \,. \quad (29)$$

Model fit statistics: number of observations 36, error degrees of freedom: 21, root mean squared error: 0.228, R-squared 0.97, adjusted R-squared: 0.95, P-value ≤ 0.001.

Figures 12-14 illustrate the effects of interaction on skin friction. Skin friction increases with increasing mixed convection, but this effect is reduced by higher suction. The plots in the middle confirm the ANOVA results. It is observed that skin friction behaviour is dominated by strong quadratic effects rather than linear effects, particularly the $\lambda : s$ interaction, which plays an important role in controlling the boundary layer.

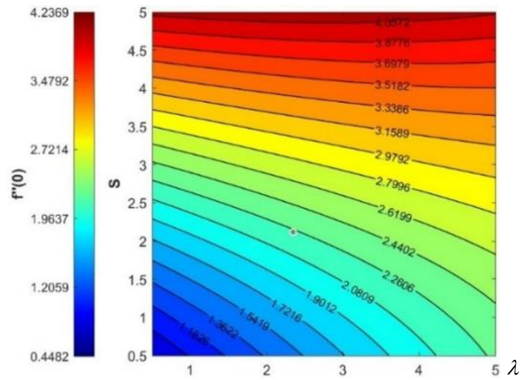

Figure 12. Contour plot for skin friction vs. s, λ.

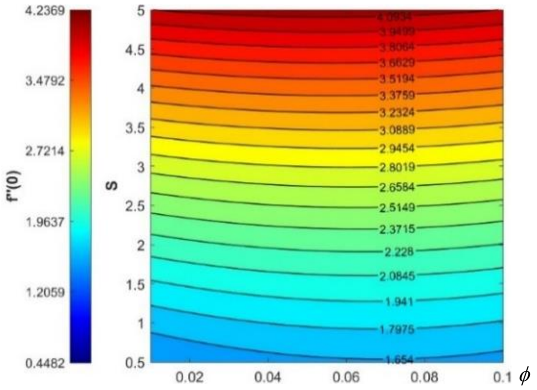

Figure 13. Contour plot for skin friction vs. s, ϕ.

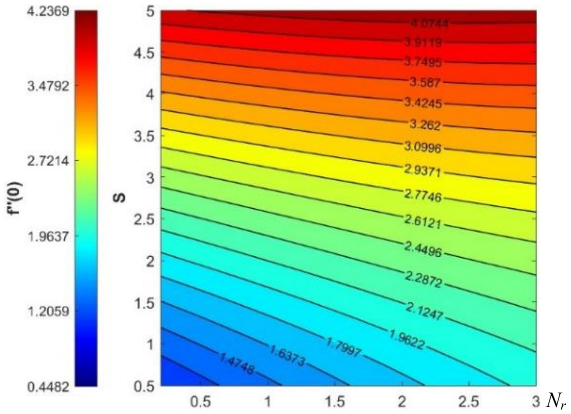

Figure 14. Contour plot for skin friction vs. s, N_r.

Table 9. Coefficients estimated for skin friction using CCD-RSM.

Term	Estimate	SE	t-Stat	P-Value
Intercept	0.1959	0.2567	0.7630	0.4539
λ	0.3697	0.1639	2.2545	0.0349
N_r	0.1698	0.2492	0.6813	0.5030
s	0.2204	0.1639	1.3445	0.1931
ϕ	5.2889	8.1993	0.6450	0.5258
$\lambda : N_r$	0.0998	0.0181	5.5145	< 0.001
$\lambda : s$	-0.0823	0.0112	-7.3117	< 0.001
$\lambda : \phi$	0.1686	0.5634	0.2993	0.7676
$N_r : s$	-0.0490	0.0181	-2.7090	0.0131
$N_r : \phi$	-0.2070	0.9055	-0.2286	0.8213
$s : \phi$	-0.1340	0.5634	-0.2379	0.8142
λ^2	-0.0175	0.0279	-0.6296	0.5356
N_r^2	-0.0304	0.0720	-0.4223	0.6770
s^2	0.1218	0.0279	4.3651	0.0002
ϕ^2	-42.8540	69.7690	-0.6142	0.5456

The regression analysis for skin friction $f''(0)$ in Table 9 depicts that the mixed convection parameter has a positive linear effect. The $\lambda : s$ interaction and the $\lambda : N_r$ interaction are the most influential factors, playing a vital role in the determination of skin friction. The volume fraction of the nanoparticle does not show a statistically significant influence. The quadratic term for suction s^2 is also highly significant having P = 0.0002, which confirms a strong nonlinear effect of suction on skin friction.

The ANOVA results in Table 10 confirm that the skin friction model is highly significant with F = 58.55 and P < 0.001, indicating that RSM model explains most of the variation compared to residual error. Linear and nonlinear terms contribute significantly to the model, confirming curvature and interaction effects. The residual error is minimal, suggesting a good fit of the model.

Table 10. ANOVA results for the skin friction response surface model.

Source	SumSq	DF	MeanSq	F	P-value
Total	43.7760	35	1.2507		
Model	42.6820	14	3.0487	58.550	< 0.001
Linear	36.1060	4	9.0266	173.350	< 0.001
Nonlinear	6.5760	10	0.6576	12.6290	< 0.001
Residual	1.0935	21	0.0521		
Lack of fit	1.0935	10	0.1094	-	0
Pure error	0	11	0		

Optimisation of system parameters

A numerical optimisation study is conducted to determine the optimal set of governing parameters for two objectives: to maximise the rate of heat transfer and minimise the skin friction of the fluid at the surface. The optimisation is performed using RSM. Optimal values derived from this analysis are shown in Tables 11 and 12.

Table 11. Parameter settings that maximise heat transfer rate.

Optimal parameter	Optimal value
Mixed convection (λ)	3.6215
Radiation (N_r)	0.2000
Suction (s)	5.0000
Volume fraction (ϕ)	0.0350
Predicted maximum Nusselt number (Nu_{max})	20.5104

Table 12. Parameter settings that minimise skin friction.

Optimal parameter	Optimal value
Mixed convection (λ)	0.5000
Radiation (N_r)	0.2000
Suction (s)	0.5000
Volume fraction (ϕ)	0.0100
Predicted minimum skin friction ($f''(0)$)	0.5827

Results of the optimised parameter depict that to maximise the Nusselt number, strong suction with weak radiation is required, which effectively enhances convective cooling. Although, to minimise skin friction, weak suction combined with low mixed convection is needed. In general, suction emerges as the dominant factor in controlling heat transfer, where maintaining low radiation consistently improves thermal performance.

CONCLUSION

Research in nanofluid flow over a shrinking sheet is paving the way for more sustainable thin film manufacture where effective cooling significantly influences the stability of the film. However, wall suction is the most influential factor in improving heat transfer and stabilising the flow, whereas high radiation parameter strongly suppresses thermal performance. Also, the mixed convection parameter affects heat transfer positively but also increases skin friction indicating a trade-off performance. This has been observed through graphical representations of temperature and velocity of current study. Finite element analysis confirms that the Nusselt number increases from 0.71 to 2.85, highlighting suction as the most effective parameter for enhancing heat transfer. The results of ANOVA confirm that our RSM model agrees with FEM results having $P < 0.001$ and $R^2 \approx 0.975$. The surface and contour plots further reveal that skin friction is primarily governed by the combined influence of suction and mixed convection. This nanofluid model offers a superior thermal efficiency compared to the basic microfluid system, making it a more effective model for applications where heat-transfer enhancement is a primary objective.

REFERENCES

1. Abbas, M.S., Qamar, M., Khan, M., Hussain, S.M. (2025), *Chemically reactive flow of Williamson nanofluid with nonlinear thermal radiation over an exponentially stretching/shrinking surface*, J Rad. Res. Appl. Sci. 18(3): 101630. doi: 10.1016/j.jrras.2025.101630
2. Abdel-Rahman Rashed, G.M., El Fayez, F.M.N. (2020), *Studying the effect of radiation on thin film sprayed nanofluid flow with heat transfer*, Heat Trans. Asian Res. 49(1): 5-17. doi: 10.1002/htj.21495
3. Algehyne, E.A., El-Zahar, E.R., Elhag, S.H., et al. (2022), *Investigation of thermal performance of Maxwell hybrid nanofluid boundary value problem in vertical porous surface via finite element approach*, Sci. Reports, 12(1): 2335. doi: 10.1038/s41598-022-06213-8
4. Alharbi, A.F., Alhawiti, M., Usman, M., et al. (2024), *Enhancement of heat transfer in thin-film flow of a hybrid nanofluid over an inclined rotating disk subject to thermal radiation and viscous dissipation*, Int. J Heat Fluid Flow, 107: 109360. doi: 10.1016/j.ijheatfluidflow.2024.109360
5. Alrehili, M. (2023), *The flow of a thermo nanofluid thin film inside an unsteady stretching sheet with a heat flux effect*, Energies, 16(3): 1160. doi: 10.3390/en16031160
6. Bhargavi, N., Poornima, T. (2025), *Investigating thermal radiation on thin films of Casson Cu-Ni-Al_2O_3/water nanofluids for enhanced solar thermal performance*, Proc. Inst. Mech. Eng., Part C: J Mech. Eng. Sci. 239(15): 6228-6237. doi: 10.1177/09544062251335545
7. Box, G.E.P., Wilson, K.B., On the Experimental Attainment of Optimum Conditions, In: Kotz, S., Johnson, N.L. (Eds.), Breakthrough in Statistics. Springer Series in Statistics, New York, NY, 1951, pp.270-310. doi: 10.1007/978-1-4612-4380-9_23
8. Chakraborty, A., Janapatla, P. (2024), *Study of Casson nanofluid flow over a wedge with variable magnetic effect, thermal radiation, and melting effects*, Num. Heat Trans. Part B: Fund. 85(10): 1437-1459. doi: 10.1080/10407790.2023.2266128
9. Evans, J.D., Palhares Junior, I.L., Oishi, C.M., Ruano Neto, F. (2025), *Analysis of Newtonian fluid flows around sharp corners with slip boundary conditions*, Theor. Comput. Fluid Dyn. 39(5): 38. doi: 10.1007/s00162-025-00756-y
10. Gonsalvesa, S., Swapnaa, G. (2023), *Heat transfer analysis using finite element method under convective boundary condition*, E3S Web Conf. 430: 01248. doi: 10.1051/e3sconf/202343001248
11. Gupta, D., Kumar, L., Bég, O.A., Singh, B. (2014), *Finite element simulation of mixed convection flow of micropolar fluid over a shrinking sheet with thermal radiation*, Proc. Inst. Mech. Eng., Part E: J Proc. Mech. Eng. 228(1): 6172. doi: 10.1177/0954408912474586
12. Hady, F.M., Ibrahim, F.S., Abdel-Gaied, S.M., Eid, M.R. (2012), *Radiation effect on viscous flow of a nanofluid and heat transfer over a nonlinearly stretching sheet*, Nanoscale Res. Lett. 7(1): 229. doi: 10.1186/1556-276X-7-229
13. Hafeez, A., Liu, D., Khalid, A. (2025), *MHD flow of radiative hybrid nanofluid across a wedge influenced by melting heat transfer: Engineering application*, Alex. Eng. J, 122: 18-27. doi: 10.1016/j.aej.2025.03.018
14. Hayat, U., Shahzad, A. (2023), *Analysis of heat transfer and thin film flow of Au-Np over an unsteady radial stretching sheet*, Num. Heat Trans., Part A: Appl. 84(11): 1338-1351. doi: 10.1080/10407782.2023.2175746
15. Ishaq, M., Ali, G., Shah, Z., et al. (2018), *Entropy generation on nanofluid thin film flow of Eyring-Powell fluid with thermal radiation and MHD effect on an unsteady porous stretching sheet*, Entropy, 20(6): 412. doi: 10.3390/e20060412
16. Hussain, Z., Kamangar, S., Arabi, A.I.A. (2025), *Numerical analysis of MHD micropolar hybrid nanofluid flow past a porous stretching sheet with slips and convective boundary conditions*, J Therm. Anal. Calorim. 150(10): 7971-7984. doi: 10.1007/s10973-025-14215-7
17. Kamis, N.I., Jiann, L.Y., Khairuddin, T.K.A., et al. (2022), *Forced convection boundary layer flow in a thin nanofluid film on a stretching sheet under the effects of suction and injection*, J Appl. Sci. Eng. 25(3): 529-535. doi: 10.6180/jase.202206-25(3).0009
18. Nabwey, H.A., Rahbar, F., Armaghani, T., et al. (2023), *A comprehensive review of non-Newtonian nanofluid heat transfer*, Symmetry, 15(2): 362. doi: 10.3390/sym15020362
19. Naseem, T., Shahzad, A. (2025), *Water based nanofluid flow and heat transfer in thin film over an unsteady stretching sheet: An entropy analysis*, Num. Heat Trans., Part A: Appl. 86(5): 1201-1225. doi: 10.1080/10407782.2023.2273453
20. Saraswathy, M., Prakash, D., Muthtamilselvan, M., Al Mdallal, Q.M. (2022), *Arrhenius energy on asymmetric flow and heat transfer of micropolar fluids with variable properties: A sensitivity approach*, Alex. Eng. J. 61(12): 12329-12352. doi: 10.1016/j.aej.2022.06.015
21. Shit, G.C., Haldar, R. (2011), *Effects of thermal radiation on MHD viscous fluid flow and heat transfer over nonlinear shrinking porous sheet*, Appl. Math. Mech.-Engl. Ed. 32(6): 677-688. doi: 10.1007/s10483-011-1448-6
22. Sohail, M., Nazir, U., Naz S., et al. (2022), *Utilization of Galerkin finite element strategy to investigate comparison performance among two hybrid nanofluid models*, Sci. Rep. 12(1): 18970. doi: 10.1038/s41598-022-22571-9
23. Ullah, A., Shah, Z., Kumam, P., et al. (2019), *Viscoelastic MHD nanofluid thin film flow over an unsteady vertical stretching sheet with entropy generation*, Processes, 7(5): 262. doi: 10.3390/pr7050262
24. Ramana Reddy, G.V., Ganteda, C., Naseem, M., et al. (2025), *Investigating the impact of thermal radiation, induced magnetic force, and convective boundary condition on MHD nanofluid flows*, J Rad. Res. Appl. Sci. 18(3): 101572. doi: 10.1016/j.jrras.2025.101572
25. Vrionis, P.Y., Demou, A.D., Karapetsas, G., et al. (2025), *An efficient and highly scalable solver for modelling thin film flows in heterogeneous environments*, Theor. Comput. Fluid Dyn. 39(5): 37. doi: 10.1007/s00162-025-00757-x
26. Yacob, N.A., Ishak, A. (2012), *Micropolar fluid flow over a shrinking sheet*, Meccanica, 47(2): 293-299. doi: 10.1007/s11012-011-9439-8
27. Zainal, N.A., Nazar, R., Naganthran, K., Pop, I. (2020), *Unsteady stagnation point flow of hybrid nanofluid past a convectively heated stretching/shrinking sheet with velocity slip*, Math. 8(10): 1649. doi: 10.3390/math8101649